JOURNAL OF THERMOPHYSICS AND HEAT TRANSFER
Vol. 13, No. 2, April–June 1999

Computational Study of Hypersonic Transitional Wake Flow

Robert P. Nance*
North Carolina State University, Raleigh, North Carolina 27695-7910
Brian R. Hollis† and Thomas J. Horvath†
NASA Langley Research Center, Hampton, Virginia 23681-0001
Stephen J. Alter‡
Lockheed Engineering and Sciences Company, Hampton, Virginia 23681-0001
and
H. A. Hassan§
North Carolina State University, Raleigh, North Carolina 27695-7910

A study of transition and turbulence in hypersonic blunt-body wake flows is presented. The current approach combines the k-ζ turbulence closure model with a newly developed transition prediction method. This method utilizes results from linear stability theory and treats transitional flows in a turbulence-like manner. As a result, the onset and extent of transition are determined as part of the solution. The model is used to study flows past two spherically blunted 70-deg cone geometries at Mach 6 and 10. Two mechanisms of instability are examined. Comparison between computation and experiment suggests that for the cases considered, transition is a result of the instability of the free shear layer emanating from the shoulder region.

Nomenclature

k = turbulent kinetic energy
M = Mach number
p = pressure
$\bar{Q}$ = Reynolds- or time-averaged value of Q
$\tilde{Q}$ = Favre-averaged value of Q
q = heat transfer rate
Re = Reynolds number
R_n = nose radius
s = linear surface distance
T = temperature
U = Velocity magnitude
u_i = velocity vector
$\tilde{x}$ = distance measured along sting support
Γ = intermittency
δ = boundary- or shear-layer thickness; k-ζ model constant
δ_{ij} = Kronecker delta
δ^* = boundary-layer displacement thickness
ζ = enstrophy
λ = transition-extent parameter
μ = dynamic viscosity
ν = kinematic viscosity
ρ = density
τ = characteristic time scale
τ_{ij} = Reynolds stress tensor
ω = transitional frequency
ω_i = vorticity vector

Subscripts
D = value based on cone diameter
l = laminar (nonturbulent) value
T = total value
t = turbulent value
tr = transitional value
1 = value at edge of shear layer
∞ = freestream

Superscripts
l = laminar value
t = turbulent value
$*$ = dimensional transitional quantity

Received June 12, 1998; presented as Paper 98-2939 at the AIAA/ASME 7th Joint Thermophysics and Heat Transfer Conference, Albuquerque, NM, June 15–18, 1998; revision received Nov. 16, 1998; accepted for publication Nov. 19, 1998. This paper is declared a work of the U.S. Government and is not subject to copyright protection in the United States.

*Research Assistant; currently Postdoctoral Fellow, Space Department, Johns Hopkins University, Applied Physics Laboratory, Baltimore, MD 21218. Member AIAA.

†Aerospace Technologist, Aerothermodynamics Branch, Aerodynamics and Gas Dynamics Division. Member AIAA.

‡Senior Aeronautical Engineer. Senior Member AIAA.

§Professor, Department of Mechanical and Aerospace Engineering. Associate Fellow AIAA.

Introduction

CURRENT and proposed planetary exploration missions, such as the recent Mars Pathfinder project, have spurred renewed interest in the physics of blunt-body wake flowfields. Accurate characterization of the near-wake environment is important for the design of entry configurations, becaues the nature of the wake closure typically places constraints on payload size and location. Recent activity in this discipline has included a number of experiments on blunt-cone models, such as the work carried out by several teams of researchers,[1–4] in support of AGARD Working Group 18 (WG 18). These WG 18 tests have been conducted in several hypervelocity facilities with the objective of characterizing the fluid dynamic phenomena present in the wake region for flows exhibiting real-gas behavior. The tests were conducted at nominally identical test conditions to help assess and quantify facility-to-facility performance. Initial comparisons of measurement with prediction indicated that the measured peak heating rates along the model sting support were two to three times greater than those predicted by laminar Navier–Stokes computations. A variety of explanations were suggested (such as flow establishment, real-gas phenomena, and wake rarefaction) to explain this disparity. Subsequent perfect-gas tests performed by Horvath et al.[5] and Horvath and Hannemann,[6] on the AGARD WG 18 geometry,

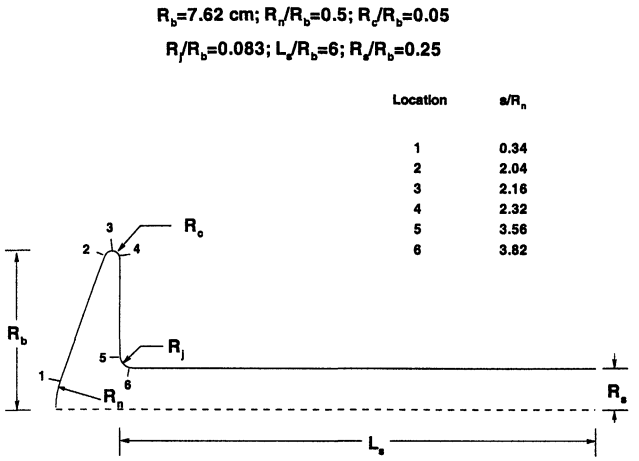

Fig. 1 Seventy-deg blunt cone and sting geometry employed in Refs. 5 and 6.

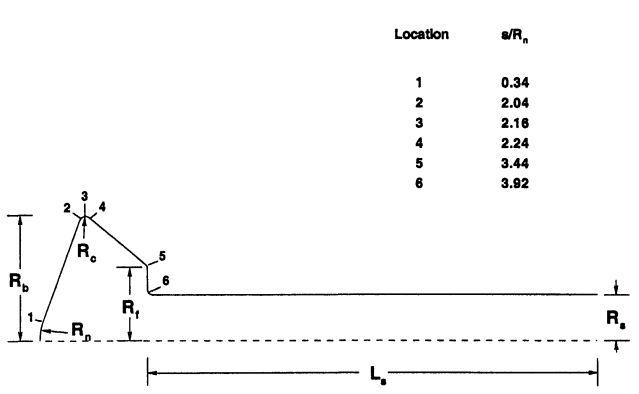

Fig. 2 Seventy-deg blunt cone and sting geometry employed by Hollis and Perkins.[7]

as well as studies by Hollis and Perkins,[7] using a similar configuration, suggested instead that wake shear-layer transition was responsible for the higher than anticipated heating levels at reattachment.

Accurate predictions of such high-speed transitional flows are important for the design of hypersonic vehicles. However, there has been little effort to date toward the development of computational tools capable of predicting transitional and turbulent flow in blunt-body wakes. Two possible mechanisms can cause transition in the wake region. These are streamwise instabilities resulting from Tollmien–Schlichting and Mack modes, and transition resulting from the instability of the free shear layer (FSL) emanating from the shoulder of the cone. The first mechanism was investigated by Nance et al.[8] for Mach 6 flows. Both mechanisms are considered in the present work, which focuses on the two configurations shown in Figs. 1 and 2 that were tested in Refs. 5–7.

Modeling Approach

This work is based on solution of the Favre-averaged Navier–Stokes equations in conjunction with a two-equation model modified for use in transitional flowfields. In this context, we seek to determine the influence of the transitional or turbulent fluctuations on the mean flow variables, instead of predicting the fluctuations themselves. Closure is obtained by specifying equations for the modeled variables, as well as expressions for disturbance-related quantities in the nonturbulent portions of the flow.

Transport Equations for Modeled Quantities

Fluctuation velocity and time scales are provided in this work by the compressible k-ζ model first proposed by Robinson et al.[9] This approach is very similar to that used in Ref. 8, with minor modifications to some of the terms and constants appearing in the model. The model constants are listed next: $C_\mu = 0.09$, $\alpha_3 = 0.35$, $\beta_4 = 0.42$, $\beta_5 = 2.37$, $\beta_6 = 0.10$, $\beta_7 = 1.50$, $\sigma_\rho = 0.065$, $\sigma_r = 0.07$, $\sigma_\rho = 65.0$, $1/\sigma_k = 1.80$, $1/\sigma_\zeta = 1.46$, $\delta = 0.10$, $C_1 = 0.60$, $C_k = 1.00$, and $C_{\zeta_1} = 2.10$. The k-ζ equation set used in this work is listed as follows:

$$\bar{\rho}\frac{Dk}{Dt} = \tau_{ij}\frac{\partial \tilde{u}_i}{\partial x_j} + \frac{\partial}{\partial x_j}\left[\left(\frac{\mu}{3} + \frac{\mu_T}{\sigma_k}\right)\frac{\partial k}{\partial x_j}\right] - C_1\frac{\bar{\rho}k}{\tau_\rho} - \frac{\bar{\rho}k}{\tau_k} - \frac{1}{C_k}\frac{\nu_T}{\bar{\rho}}\frac{\partial \bar{\rho}}{\partial x_k}\frac{\partial \bar{p}}{\partial x_k} \tag{1}$$

$$\bar{\rho}\frac{D\zeta}{Dt} = \frac{\mu_T}{\sigma_r}\frac{\partial \tilde{\omega}_i}{\partial x_j}\left[\left(\frac{\partial \tilde{\omega}_i}{\partial x_j} + \frac{\partial \tilde{\omega}_j}{\partial x_i}\right)\right] + \frac{\partial}{\partial x_j}\left[\left(\mu + \frac{\mu_T}{\sigma_\zeta}\right)\frac{\partial \zeta}{\partial x_j}\right] - \frac{\beta_5}{\sqrt{R_t + \delta}}\bar{\rho}\zeta^{3/2} + \left(\alpha_3 b_{ij} + \frac{1}{3}\delta_{ij}\right)\bar{\rho}\zeta\tilde{s}_{ij} - \frac{\beta_4\zeta\tau_{ij}\tilde{\omega}_i\tilde{\omega}_j}{k\tilde{\omega}} - \frac{2\beta_6\tau_{ij}\nu_T}{k\nu}\tilde{\omega}\tilde{\omega}_i\tilde{\omega}_j + \frac{\beta_7\bar{\rho}\zeta}{\tilde{\omega}^2}\tilde{\omega}_i\tilde{\omega}_j\tilde{s}_{ij} + \max(P_\zeta, 0) - \frac{C_{\zeta_1}\mu_T\zeta\tilde{\omega}}{k\tau_\rho} - 2\bar{\rho}\zeta\tilde{s}_{kk} \tag{2}$$

where

$$\tau_{ij} = \mu_T\left(2\tilde{s}_{ij} - \frac{2}{3}\delta_{ij}\tilde{s}_{kk}\right) - \frac{2}{3}\delta_{ij}\bar{\rho}k, \qquad b_{ij} = \frac{\tau_{ij} + \frac{2}{3}\bar{\rho}k\delta_{ij}}{\bar{\rho}k}$$

$$s_{ij} = \frac{1}{2}\left(\frac{\partial \tilde{u}_i}{\partial x_j} + \frac{\partial \tilde{u}_j}{\partial x_i}\right), \qquad k = \frac{1}{2}u_k''u_k'', \qquad \zeta = \omega_k''\omega_k''$$

$$R_t = \frac{k^2}{\nu^2\zeta}, \qquad \nu_T = \frac{\mu_T}{\bar{\rho}}, \qquad P_\zeta = \bar{\rho}\frac{D\bar{p}}{Dt}\frac{k\tilde{\omega}}{\nu\bar{p}\sigma_\rho}\frac{1}{(1+\delta_\rho)}$$

$$\delta_\rho = \frac{\sigma_\rho}{\bar{\rho}}\sqrt{\frac{2kR_t}{\zeta}\left(\frac{\partial \bar{\rho}}{\partial x_k}\right)^2}, \qquad \frac{1}{\tau_\rho} = \frac{1}{\bar{\rho}}\sqrt{k\left(\frac{\partial \bar{\rho}}{\partial x_k}\right)^2}$$

Specific alterations to the k-ζ equation set include reformulation of the density-gradient time scale and reduction of the pressure-work constant C_k. These modifications were made to preserve Galilean invariance while maintaining good agreement with experimental data when applied to transonic airfoils. Note that the Reynolds stress tensor is modeled using the Boussinesq approximation. Preliminary investigations of these flowfields employing a partial differential stress model,[10] wherein the Reynolds normal stresses are predicted using model transport equations, yielded no improvement in predictions when compared with the Boussinesq approach.

Instability Mechanism

An advantage of the k-ζ formulation is that the model terms are derived without explicitly declaring the nature of the fluctuation. Hence, the model may be used to predict the entire flowfield, including transitional and fully turbulent regions, provided an appropriate stress–strain relation is employed. Such a relationship is obtained in part by defining the total eddy viscosity in terms of a fully turbulent contribution and a contribution as a result of nonturbulent fluctuations:

$$\mu_T = (1 - \Gamma)\mu_{tr} + \Gamma\mu_t \tag{3}$$

Equation (3) can be rewritten as a combination of terms of nonturbulent and fully turbulent time scales as follows:

$$\mu_T = C_\mu \bar{\rho} k \tau_\mu \tag{4}$$

$$\tau_\mu = (1 - \Gamma)\tau_\mu^l + \Gamma \tau_\mu^t \tag{5}$$

The fully turbulent time scale is given as

$$\tau_\mu^t = k/v\zeta \tag{6}$$

The nonturbulent time scale is dictated by the mechanism responsible for transition. In Ref. 8, nonturbulent disturbances were considered through a model accounting for Mack's[11] first and second modes. Hence, the nonturbulent characteristic time scale was originally defined as

$$\tau_\mu^l = \tau_1 + \tau_2 \tag{7}$$

where the two time scales are defined in terms of first- and second-mode characteristic frequencies, and the frequencies are correlated as

$$\tau_1 = a/\omega_{TS}, \qquad \tau_2 = b/\omega_{SM} \tag{8}$$

$$\omega_{TS}\nu/U_e^2 = 3.2Re_{\delta^*}^{-3/2} \tag{9}$$

$$\omega_{SM} = U_p/2\delta \approx (U_p/M_e^2)\sqrt{Re_e/s} \tag{10}$$

where U_p, the phase velocity, is taken to be 0.94 times the edge velocity U_e. A second possible cause of transition is a result of instability of the FSL emanating from the shoulder of the cone. Such FSLs are always unstable. The most amplified frequency, which is required for the present formulation, is obtained from linear stability theory predictions for compressible mixing layers.[12] For all of the Reynolds numbers, Mach numbers, and velocity ratios considered in Ref. 12, the nondimensional value of the most amplified frequency was found to be relatively invariant, always falling in the range $\omega = 0.05-0.15$. This nondimensional frequency is related to the dimensional value by

$$\omega^* = \omega U_1^*/\delta^* \tag{11}$$

where U_1 is the velocity of the higher-velocity stream, and δ^* is proportional to the thickness of the layer:

$$\delta^* = \sqrt{\mu_1^* \tilde{x}^*/\rho_1^* U_1^*} \tag{12}$$

x^* represents the dimensional distance from the start of the mixing layer, which in this case is taken to correspond to distance along the sting support. The dimensional frequency can be used to define the nonturbulent characteristic time scale:

$$\tau_\mu^l = d/\omega^* \tag{13}$$

For the present work, the nondimensional frequency appearing in Eq. (11) is taken as 0.10, and the model constant d is chosen as 5.0. The dissipation term in the k equation is also modified to account for transitional effects by computing the representative decay time for turbulent kinetic energy as

$$1/\tau_k = [(1 - \Gamma)/\tau_k^l] + (\Gamma/k_k^t) \tag{14}$$

where

$$1/\tau_k^l = C(\nu_T/\nu)\tilde{s}, \qquad \tau_k^t = \tau_\mu^t, \qquad \tilde{s}^2 = \tilde{s}_{ij}\tilde{s}_{ij}$$

and the model constant C is chosen as 0.01. While a more rigorous approach would correlate ω with parameters such as Mach number and Reynolds number, there is insufficient data for performing such a correlation at present.

Transition Prediction and Intermittency Calculation

As in Ref. 8, we chose the transition onset location as the location of minimum shear stress along the sting. The minimum heat-flux criterion proposed earlier is not considered here, because it was found to yield poorer agreement with available data. A criterion based on the location of flow reattachment along the sting was also considered, but it was discarded because it also yielded degraded comparisons.

The intermittency correlation, owed to Dhawan and Narasimha,[13] is retained from the previous work:

$$\Gamma = 1 - \exp(-0.412\xi^2) \tag{15}$$

However, the intermittency determination in Ref. 8 utilized a distance parameter ξ based on a linear surface distance starting from the forward stagnation point. In keeping with the notion of shear-layer instability, the parameter ξ is now based on distance along the sting. That is,

$$\xi = \max(\tilde{x} - \tilde{x}_t, 0)/\lambda \tag{16}$$

where

$$Re_\lambda = 9.0Re_{\tilde{x}_t}^{0.75} \tag{17}$$

and the Reynolds numbers appearing in Eq. (17) are based on conditions at the edge of the layer. In Eq. (16), $\tilde{x}_t$ is the location of transition onset, and is determined as part of the solution to correspond to the location of minimum skin friction along the sting.

Model Constants

One of the test cases ($M = 6$, $Re = 2 \times 10^6$) was used to calibrate model constants, i.e., b, d, and C appearing in Eqs. (8), (13), and (14). Heat transfer calculations in the base and sting regions were used to determine best choices for these model constants. Figure 3 shows heat transfer calculations in the base plane and sting regions for the streamwise disturbance (SD) and FSL transition models and experiment. The resulting model constants, which were specified earlier, are used for the other cases considered in this work. The figure indicates, in addition, that laminar calculations underpredict heat transfer measurements by a wide margin.

Numerical Method

The modeling proposed here has been incorporated into Olynick and Hassan's[14] two-dimensional/axisymmetric im-

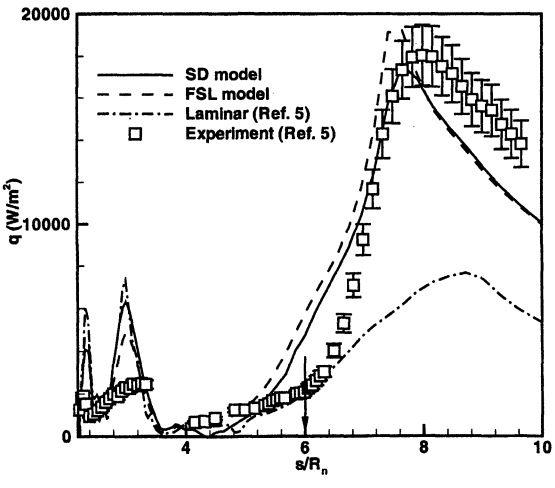

Fig. 3 Comparison of base plane/sting heating results for case 2.

plicit solver for hypersonic flows. This algorithm solves the governing equations for five-species air in thermochemical nonequilibrium. The solver uses Roe's[15] flux-difference splitting for the inviscid flux, extended to higher order using a monotone upstream-centered schemes for conservation laws (MUSCL) variable extrapolation[16] with a minmod slope limiter. Time integration is accomplished using the diagonal implicit variant of Yoon and Jameson's[17] lower–upper symmetric Gauss–Seidel method, which only requires the inversion of diagonal matrices. This property is attractive for nonequilibrium flows, where a large number of partial differential equations must be solved.

Because the current flowfields under investigation are perfect-gases, vibrational relaxation and chemical reactions are disabled to obtain the results in this study. Additionally, the high-temperature transport-property calculations originally used in the code were replaced with Sutherland's law for viscosity and a constant laminar Prandtl number of 0.72. Closure for the Favre-averaged energy equation is accomplished using a constant turbulent Prandtl number of 0.89.

To promote physically realizable solutions, the computed values of k and ζ are required to remain positive throughout the computational domain. However, no artificial limitation on turbulent kinetic energy production was imposed in the numerical method. Transitional solutions are started by running the solver in a laminar-flow mode for about 100 iterations.

Results and Discussion

Two blunt cone configurations are considered. Test results for the first configuration are available at Mach 6 and 10, whereas only Mach 10 data are available for the second configuration. The freestream conditions for cases considered together with the grids employed are presented in Table 1. Because no data are available regarding the freestream disturbance intensity in either NASA Langley Research Center's 20-ft Mach 6 or 31-ft Mach 10 facilities, freestream intensities of 0.3 and 0.9%, respectively, were assumed. Additionally, the wall temperature is fixed at 300 K.

Forebody

Laminar calculations[5–7] for the cases considered here indicate that the flow on the forebody is essentially laminar. Moreover, present transition/turbulence models indicate that minimum skin friction occurs on the sting. Figures 4–6 compare laminar calculations together with present calculations for the two transition models under consideration for case 2 (see Table 1) in Fig. 4, and cases 4 and 5 in Figs. 5 and 6. Grid 1 (Table 1) is used for the present calculations. The laminar calculations for these cases all employed a 193 × 76 grid that was very similar to grid 1. In general, good agreement is indicated. The present calculations yield somewhat higher forebody heating predictions than the laminar calculations; these differences may be attributed to differences in inviscid-flux parameters such as eigenvalue limiters and higher-order extrapolation.

Comparison of Transition Mechanisms

The role of transition mechanism will be discussed for cases 1 and 3–6. In the figures to follow, results for the two disturbance models considered are compared with the laminar calculations and experiment[5–7] for the base plane and sting regions. All calculations for these comparisons were carried out on grid 1 (Table 1).

Figure 7 compares computed results for case 1 ($M = 6$, $Re_D = 0.5 \times 10^6$) with experiment. The geometry is that indicated in Fig. 1. The horizontal axis begins at $s/R_n = 2.2$. This location corresponds to a point just downstream of the apex of the shoulder. For this case, both models compare reasonably well with the experimental heat transfer data along the sting. However, the SD model yields a lower heating magnitude. Both mechanisms predict a peak heating location upstream of that observed in the measurements. Predicted onset locations, which correspond to minimum skin friction, are denoted in the figure by the vertical lines near the horizontal axis.

Examination of the local heating maxima along the base plane shows that the SD model predicts higher heating in this

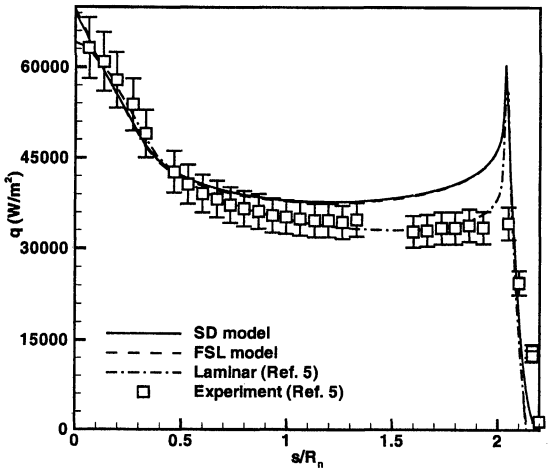

Fig. 4 Comparison of forebody heating results for case 2.

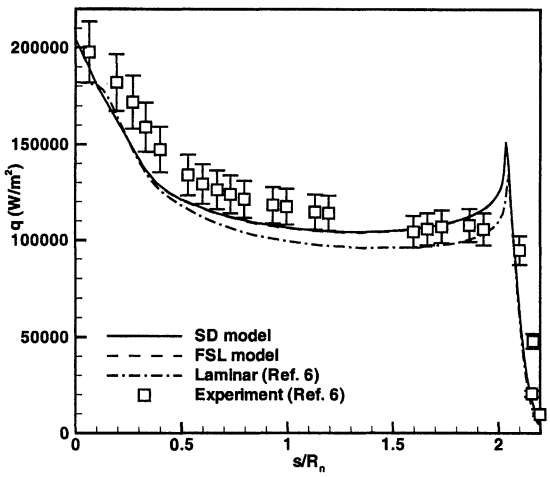

Fig. 5 Comparison of forebody heating results for case 4.

Table 1 Freesteam conditions and grid dimensions[5–7]

Geometry	Case 1, Fig. 1	Case 2, Fig. 1	Case 3, Fig. 1	Case 4, Fig. 1	Case 5, Fig. 2	Case 6, Fig. 2
Re_D	0.5×10^6	2×10^6	2.8×10^5	1×10^6	8.23×10^4	3.15×10^5
ρ_∞, kg/m^3	1.68×10^{-2}	6.45×10^{-2}	4.471×10^{-3}	1.613×10^{-2}	4.51×10^{-3}	1.646×10^{-2}
U_∞, m/s	931	943.8	1415	1426	1416	1425
T_∞, K	63.3	61.27	53.15	51.27	53.31	51.48
M_∞	6	6	10	10	10	10
Grid 1	189 × 75	189 × 75	189 × 75	189 × 75	125 × 90	125 × 90
Grid 2	377 × 149	377 × 149	377 × 149	377 × 149	249 × 179	249 × 179
Grid 3	——	——	505 × 149	——	333 × 179	——

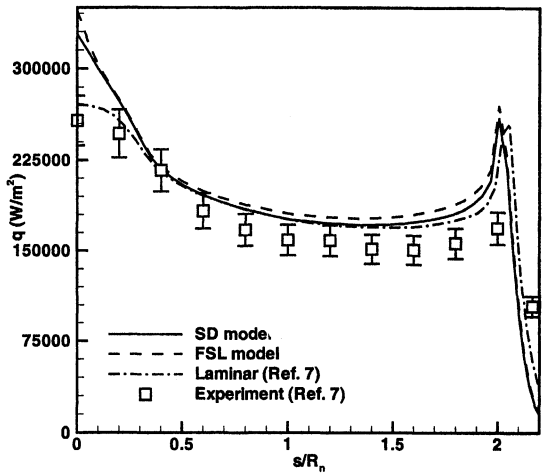

Fig. 6 Comparison of forebody heating results for case 6.

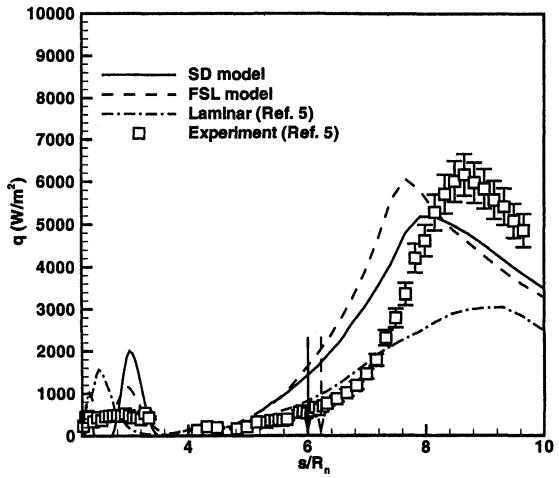

Fig. 7 Comparison of base plane/sting heating results for case 1.

region. Because the flow is unsteady as a result of the presence of separation bubbles, local time stepping may not be appropriate to determine the mean heat flux measured in the experiment. Even the laminar calculations indicate heating rates higher than experiment in this region.

Figures 8 and 9 compare computations for cases 3 and 4, respectively ($M = 10$, $Re_D = 2.8 \times 10^5$, 1×10^6, respectively) with experiment. Again, the geometry is indicated in Fig. 1. Examination of the two figures show that computational trends are the same as those described earlier for Fig. 7. The figures indicate that peak heating increases with Reynolds number. Although the predictions indicated in Fig. 9 are reasonable, neither model compares well with the experimentally measured peak heating in Fig. 8. Although the FSL model offers slightly higher peak heating, it still differs by roughly 30% from the peak in the data. The reason for the poor agreement in this case is unclear. Moreover, it is somewhat puzzling because, as is seen in the following text, agreement is good for cases that are characterized by similar and lower freestream Reynolds numbers.

Figures 10 and 11 compare computations for cases 5 and 6, respectively ($M = 10$, $Re_D = 8.23 \times 10^4$, 3.15×10^5, respectively). For these figures, the geometry is that as indicated in Fig. 2. As seen from the figures, the FSL model compares more favorably to the data than does the SD model. Although the peak heating is well predicted by the FSL model, the location of the peak heating is better predicted by the SD model. As expected, the laminar solution is in good qualitative agreement with experiment at the lowest Reynolds numbers. Note that the kinks in the sting heating prediction for cases 5 and 6 arise from a slope discontinuity in the wake region grid lines. These kinks do not indicate, in any way, convergence difficulties.

Note that cases 3 and 6 have approximately the same Reynolds number. The fact that good agreement is indicated for case 6 and the other cases, with the exception of case 3, suggests that the discrepancy for case 3 is not a result of the inadequacy of the transition models.

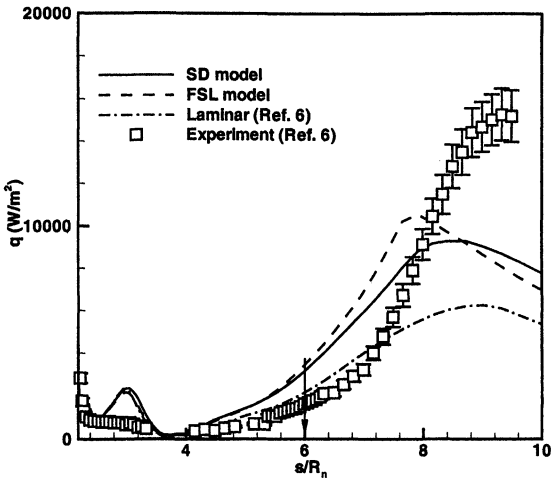

Fig. 8 Comparison of base plane/sting heating results for case 3.

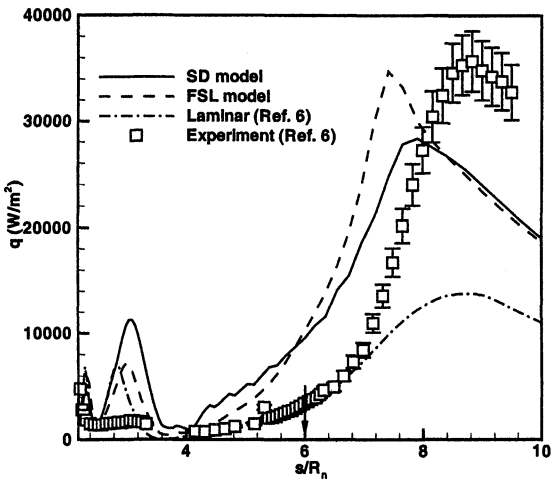

Fig. 9 Comparison of base plane/sting heating results for case 4.

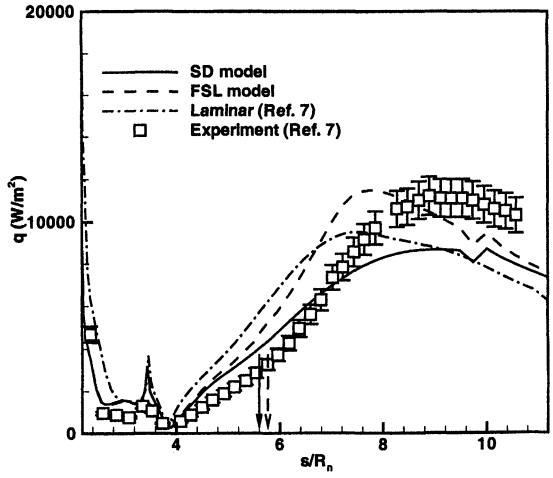

Fig. 10 Comparison of base plane/sting heating results for case 5.

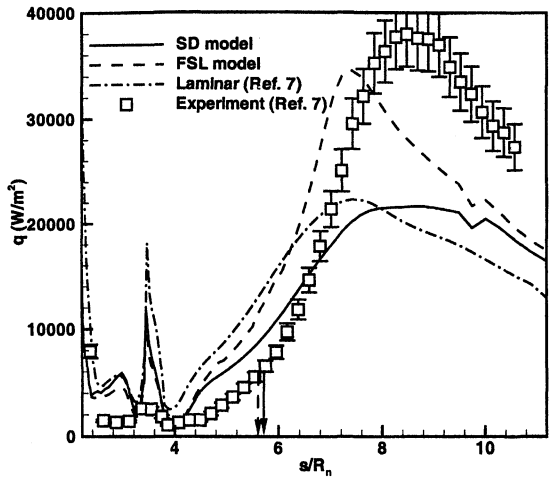

Fig. 11 Comparison of base plane/sting heating results for case 6.

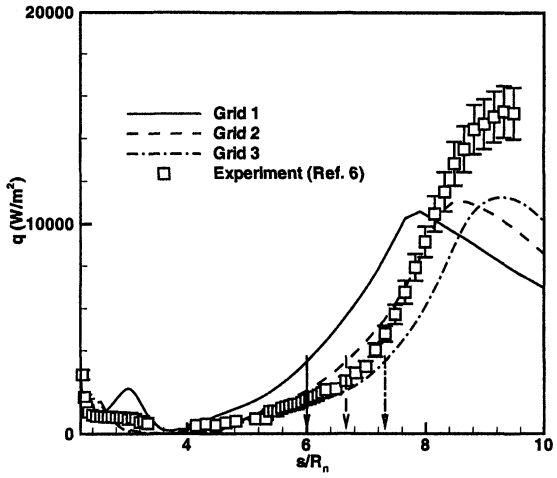

Fig. 12 Influence of grid refinement for case 3.

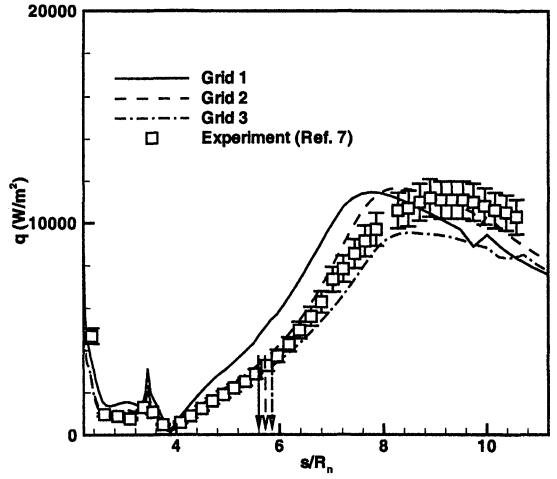

Fig. 13 Influence of grid refinement for case 5.

Grid Refinement Studies

Because of the difficulties encountered with case 3, attention is focused next on grid refinement studies. We confine our attention to solutions using the FSL disturbance model because it provides a more favorable overall agreement for the cases considered here. Also, comparisons will be limited to base plane and sting region.

Figures 12 and 13 present grid studies for cases 3 and 5. The finest grids were obtained using the volume grid manipulator package,[18] which attempts to concentrate points in regions of the highest gradients. For all grid refinement studies presented here, the refined grid predicted a later transition onset. The movement is accompanied by an observed shift of the peak heat flux which brings predictions in better agreement with experiment. The reason for this is that the recirculation region in the wake is better resolved, consistently leading to a flow reattachment point farther downstream along the sting. Consequently, the location of the minimum shear stress is also shifted rearward, leading to delayed transition. Figure 12 demonstrates that refinement results in a slight increase in peak heating. This is different from the result indicated in Fig. 13. Figure 13 also shows that grid refinement does not explain the discrepancy between the predictions and experiments for case 3. Further grid-refinement studies for the Mach 10 cases are discussed in Ref. 19.

Concluding Remarks

The combination of transition and turbulence models used in this work was shown to provide improved agreement between the numerical heat transfer predictions and available experimental data for the cases considered. In general, the present method yielded good comparisons to the experimental sting heating data for a wide range of freestream Reynolds numbers.

Coarse-grid solutions produced good predictions of the magnitude of the peak sting heating rates, although the locations of these peaks were consistently predicted upstream of the peaks observed in the measurements. Increasing grid resolution, however, tended to improve the agreement even more by shifting the predicted peak locations farther downstream.

The overall agreement between computation and data for the transitional-flow approach described herein is much better than that seen in laminar computations for the same flow conditions. This improvement lends support to the notion that transition to turbulence does occur in the blunt-body flows examined here.

Acknowledgments

This work was supported in part by NASA Cooperative Agreement NCC1-112 and a Graduate Assistance in Areas of National Need Computational Engineering and Sciences Fellowship. The authors wish to thank Klaus Hannemann at DLR, German Aerospace Research Center, for supplying the computational grids for cases 1 and 2. Supercomputer resources were provided by the North Carolina Supercomputing Center.

References

[1]Holden, M., Kolly, J., and Chadwick, K., "Calibration, Validation and Evaluation Studies in the LENS Facility," AIAA Paper 95-0291, Jan. 1995.

[2]Kastell, D., Horvath, T. J., and Eitelberg, G., "Nonequilibrium Flow Expansion Experiment Around a Blunted Cone," *Proceedings of the 2nd European Symposium on Aerothermodynamics for Space Vehicles*, European Space Agency, Paper SP-367, Norwijk, The Netherlands, 1995.

[3]Gochberg, L. A., Allen, G. A., Gallis, M. A., and Deiwert, G. S., "Comparison of Computations and Experiments for Nonequilibrium Flow Expansions Around a Blunted Cone," AIAA Paper 96-0231, Jan. 1996.

[4]Muylaert, J., Walpot, L., Speel, M., Tumino, G., and Steijl, R., "Nonequilibrium Computational Analysis of Blunt-Cone Experiments Performed in the LENS and HEG Facilities," AIAA Paper 96-2436, June 1996.

[5]Horvath, T. J., McGinley, C. B., and Hannemann, K., "Blunt Body near Wake Flow Field at Mach 6," AIAA Paper 96-1935, June 1996.

[6]Horvath, T. J., and Hannemann, K., "Blunt Body near Wake Flow Field at Mach 10," AIAA Paper 97-0986, Jan. 1997.

[7]Hollis, B. R., and Perkins, J. N., "Transition Effects on Heating in the Wake of a Blunt Body," AIAA Paper 97-2569, June 1997.

[8]Nance, R. P., Horvath, T. J., and Hassan, H. A., "Transition and Turbulence Modeling for Blunt-Body Wake Flows," AIAA Paper 97-2570, Jan. 1997.

[9]Robinson, D. F., Harris, J. E., and Hassan, H. A., "Unified Turbulence Closure Model for Wall Bounded and Free Shear Flows,"

AIAA Journal, Vol. 33, No. 12, 1995, pp. 2325–2331.

[10]Nance, R. P., and Hassan, H. A., "Turbulence Modeling of Shock-Dominated Flows with a k-ζ Formulation," AIAA Paper 99-0153, Jan. 1999.

[11]Mack, L. M., "Boundary-Layer Linear Stability Theory," AGARD Rept. 709, June 1984.

[12]Ragab, S. A., and Wu, J. L., "Linear Instabilities in Two-Dimensional Compressible Mixing Layers," *Physics of Fluids A*, Vol. 1, No. 6, 1989, pp. 957–966.

[13]Dhawan, S., and Narasimha, R., "Some Properties of Boundary Layer Flow During Transition from Laminar to Turbulent Motion," *Journal of Fluid Mechanics*, Vol. 3, No. 4, 1958, pp. 418–436.

[14]Olynick, D. P., and Hassan, H. A., "A New Two-Temperature Dissociation Model for Reacting Flows," *Journal of Thermophysics and Heat Transfer*, Vol. 7, No. 4, 1993, pp. 687–696.

[15]Roe, P. L., "Approximate Riemann Solvers, Parameter Vectors and Difference Schemes," *Journal of Computational Physics*, Vol. 43, 1981, pp. 357–372.

[16]Van Leer, B., "Towards the Ultimate Conservative Difference Scheme. V. A Second Order Sequel to Godunov's Method," *Journal of Computational Physics*, Vol. 32, No. 1, 1979, pp. 101–136.

[17]Yoon, S., and Jameson, A., "An LU-SSOR Scheme for the Euler and Navier-Stokes Equations," AIAA Paper 87-0600, Jan. 1987.

[18]Alter, S. J., "Complex Volume Grid Generation Through the Use of Grid Reusability," AIAA Paper 97-1987, June 1997.

[19]Nance, R. P., Hollis, B. R., Horvath, T. J., and Hassan, H. A., "Solution of Transitional Wake Flows at Mach 10," AIAA Paper 98-2939, June 1998.